

# Evolution of Colloidal Nanocrystals: Theory and Modeling of their Nucleation and Growth

## Supporting Information

Joel van Embden,<sup>†</sup> John E. Sader,<sup>‡</sup> Malcolm Davidson,<sup>¶</sup> and Paul Mulvaney<sup>\*,†</sup>

*School of Chemistry and Bio21 institute, University of Melbourne, Parkville, VIC, 3010, Australia., Department of Mathematics and Statistics, University of Melbourne, Parkville, VIC, 3010, Australia., and Department of Chemical and Biomolecular Engineering, University of Melbourne, Parkville, VIC, 3010, Australia.*

E-mail: mulvaney@unimelb.edu.au

### Nanocrystal Growth Rate

Figure S-1 shows three plots of the dimensional instantaneous growth rate (GR) as a function of crystal radius. Panel A displays the growth rate calculated for different values of the Damköhler number ranging from 0.001 to 1000 with  $S=100$  and  $\gamma = 0.2Jm^{-2}$ . We see that as  $\xi$  is decreased within this range, the GR increases over several orders of magnitude. At  $\xi = 1000$ , growth is reaction limited and the GR varies with radius only for the smallest crystal sizes. Within the framework of the imposed conditions at  $\xi = 0.01$  the GR has reached the diffusion limit. Further decreases to  $\xi$  have little effect on the magnitude of the rate. At low values of  $\xi$  the rate of crystal

---

\*To whom correspondence should be addressed

<sup>†</sup>University of Melbourne

<sup>‡</sup>University of Melbourne

<sup>¶</sup>University of Melbourne

growth is highly sensitive to its radius. It should be noted that changing the ratio of diffusion to reaction limited growth has no effect on the size of the crystals with a zero growth rate.

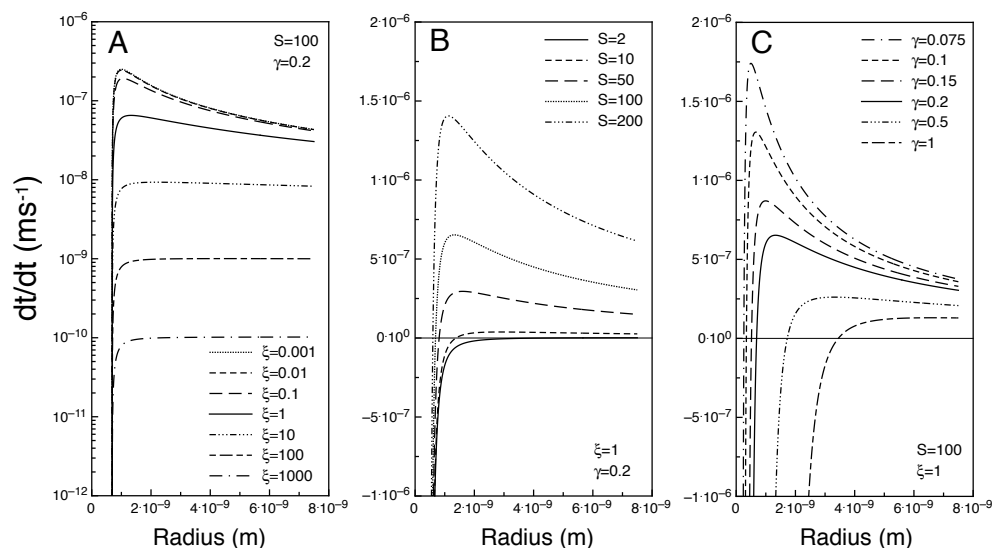


Figure S-1: Effects of  $\xi$  (A),  $S$  (B) and  $\gamma$  (C) on the instantaneous growth rate. The above growth rates were simulated using the following constants:  $V_m = 3.29 \times 10^{-5} \text{ m}^3 \text{ mol}^{-1}$ ,  $D = 1 \times 10^{-11} \text{ m}^2 \text{ s}^{-1}$ ,  $T = 500 \text{ K}$ ,  $[C]_{\infty}^0 = 0.1 \text{ mol m}^{-3}$ .

In Panel B we set  $\gamma = 0.2 \text{ Jm}^{-2}$  and  $\xi = 1$  and varied the supersaturation,  $S$ , from 2 to 200. As expected, increasing  $S$  increases the GR. By increasing  $S$  we increase the flux of monomer toward the particle surface. Hence, for intermediate values of  $\xi$ , where the GR is still reasonably sensitive to changes in the concentration gradient across the diffusion sphere, we see a change in the functional form of the GR from a reaction to a diffusion limited type profile upon increasing  $S$ . Furthermore, increasing  $S$  increases the range of crystals with a positive GR.

In Panel C we vary  $\gamma$  for a constant value of  $S$  and  $\xi$ . Increasing  $\gamma$  from  $0.075 \text{ Jm}^{-2}$  to  $1 \text{ Jm}^{-2}$  the radius of the crystals with a ZGR increases from c.a.  $0.25 \text{ nm}$  to  $2.2 \text{ nm}$ , which defines the smallest achievable NCs. Through the exponential term,  $\gamma$  has a massive effect on the instantaneous  $[C]_e$  for the crystals. Similar to the trends observed for increasing  $S$ , a drastic reduction to  $[C]_e$  at low  $\gamma$  materialises by increasing the driving force for growth across all crystal sizes. It is important to note that the sensitivity of the functional form of the GR to changes in either  $S$  or  $\gamma$  is evident only at intermediate values of  $\xi$ , with this sensitivity diminishing in either the reaction or diffusion limits.

## Nanocrystal Nucleation Rate

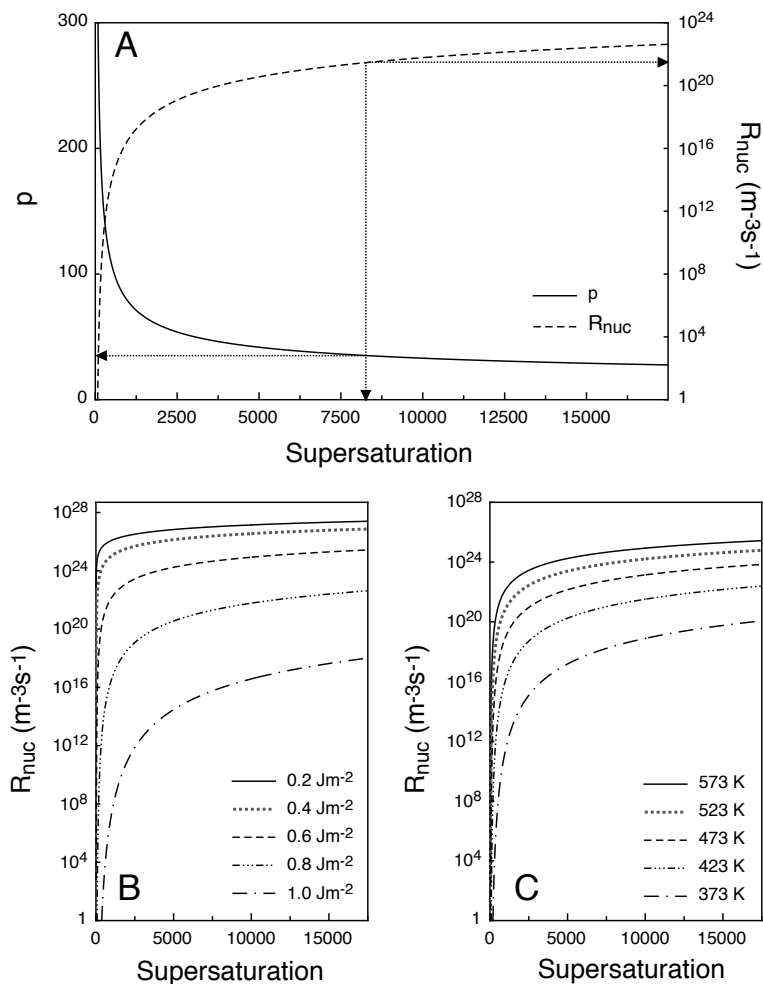


Figure S-2: (A) Nucleation rate and the corresponding  $p$  value in solution as a function of supersaturation with  $T = 573K$ ,  $u = 0.46$ ,  $r_m = 1.87 \times 10^{-10}m$ ,  $D = 1 \times 10^{-10}m^{-2}s^{-1}$ ,  $[C]_{\infty}^0 = 1 \times 10^{-3}molm^{-3}$  and  $\gamma = 0.6Jm^{-2}$ . (B) and (C) Nucleation rates as a function of supersaturation for varying values of  $\gamma$  ( $T = 573K$ ) and  $T$  ( $\gamma = 0.6Jm^{-2}$ ) respectively.

Figure S-2A is plot of the number of monomer units in the critical cluster and the corresponding nucleation rate as a function of  $S$ . We see that at low supersaturations a small increase in  $S$  results in a dramatic reduction to  $p$ . As  $S$  is further increased  $p$  decreases monotonically and at  $S \sim 100$  the nucleation rate begins to increase in magnitude. The arrows indicate a nucleation rate of  $5 \mu Ms^{-1}$ , which corresponds to a supersaturation of  $\sim 8300$  ( $8.3 molm^{-3}$ )<sup>1</sup> and a  $p$  value of  $\sim 32$ . The sensitivity of  $R_{nuc}$  to  $S$  and  $\gamma$  is best viewed in Panel B, which shows the nucleation rate as a

<sup>1</sup>Typical monomer concentrations in the range 20-60  $molm^{-3}$  are employed for nanocrystal synthesis.

function of  $S$  for different values of  $\gamma$ . For a surface energy of  $0.2 \text{ Jm}^{-2}$  increasing  $S$  from 2 to 200 results in an increase in the number of nucleated particles per cubic metre per second from  $3 \times 10^8$  to  $2 \times 10^{25}$ . The responsiveness of  $R_{nuc}$  to  $S$  drops as  $\gamma$  is increased. By raising  $\gamma$  from  $0.2 \text{ Jm}^{-2}$  to  $1 \text{ Jm}^{-2}$  the onset of nucleation requires an  $S$  value of c.a 418 compared to 1.7. Panel C displays a plot of the nucleation rate as a function of  $S$  at different reaction temperatures ( $\gamma=0.6 \text{ Jm}^{-2}$ ). As  $T$  is decreased from  $573 \text{ K}$  to  $373 \text{ K}$   $R_{nuc}$  drops off significantly. A solution with an  $S$  value of 215 at  $373 \text{ K}$  will nucleate  $\sim 10$  particles per metre cubed per second compared with  $6 \times 10^{18}$  at  $573 \text{ K}$ . Under standard laboratory conditions a supersaturation of 2000 would be required to nucleate just one single particle per second per cubic metre.

### **Effects of initial stationary distribution function**

Here we evaluate the effects of the initial distribution function ( $g(r)$ ) on the evolution of NCs over time under various reaction conditions. Both test simulations were conducted in the reaction limit  $\xi = 1 \times 10^6$  as appropriate to the nucleation and growth of NCs. Three different initial distributions were trialed under otherwise identical reaction conditions, namely: A distribution where the number of particles continually increases below the critical radius (A), a negatively skewed distribution (B) and a Gaussian distribution (C). From inspection of Figure S-3 it can be seen that despite the form of the initial stationary distribution ( $t = 0$ ) after  $250 \text{ ms}$  all the distributions begin to appear Gaussian in nature. By  $t = 3 \text{ s}$  all the distributions have converged and are almost indistinguishable. Notably  $\sim 3 \text{ s}$  is approximately the time taken for injection and mixing in typical hot injection protocols. It is also evident from the distributions at  $t = 3 \text{ s}$  that the mean radius and particle number ([NCs]) have also converged to similar values. Furthermore, from comparison of Test Simulations 1 and 2 we see that the insensitivity of the simulation outcome to the choice of distribution function is preserved for different supersaturations and surface energies. In summary, these simulations have shown that regardless of form of the initial distribution function (and reaction conditions) the distributions converge to Gaussian-type within the injection/mixing time of hot injection protocols.

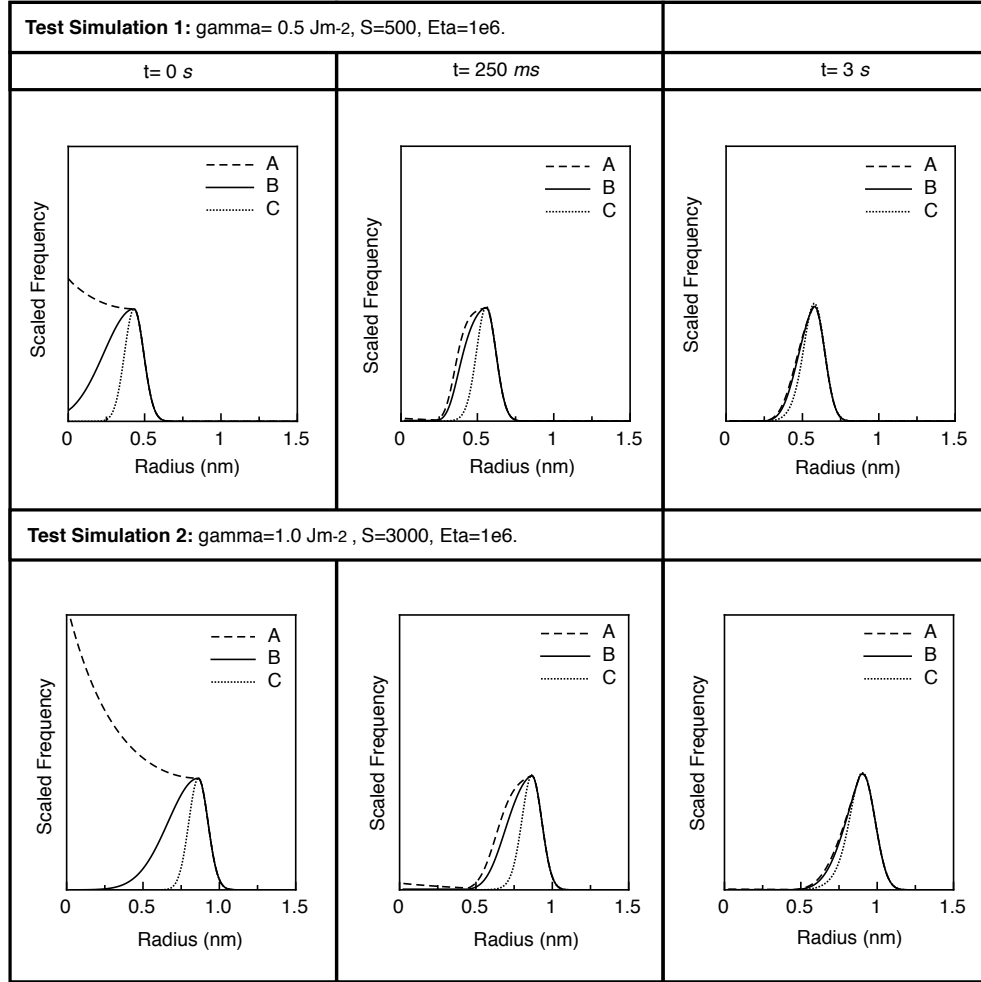


Figure S-3: Test simulations highlighting the insensitivity of a given simulation to the choice of initial distribution function. The distributions used are: A distribution where the number of particles continually increases below the critical radius (A-dashed line), a negatively skewed distribution (B-solid line) and a Gaussian distribution (C-dotted line).

## Flux Limiter Functions

In this section we present the results of test simulations using various flux limiter functions applied to the advection of both Gaussian and step-functions. The limiter functions  $\Psi(\chi)$  used are given by:

$$\Psi(\chi) = \frac{\chi + |\chi|}{1 + \chi} \quad \text{VanLeer}(\chi), \quad (1)$$

$$\Psi(\chi) = \frac{(\chi + \chi^2)}{(1 + \chi^2)} \quad \text{VanAlbada}(\chi) , \quad (2)$$

$$\Psi(\chi) = \text{Max}\{0, \text{Min}[1, 2\chi]\} \quad \text{MinMod}(\chi) , \quad (3)$$

$$\Psi(\chi) = \text{Max}\{0, \text{Min}[2\chi, 1], \text{Min}[\chi, 2]\} \quad \text{Superbee}(\chi) . \quad (4)$$

Prior to the implementation of a numeric scheme it is vital to test its stability and accuracy. This not only ensures that the written code is stable but also gives valuable information regarding the extent of total error associated with the implemented scheme due to *round-off* and *truncation errors*.<sup>2</sup> In order to test these properties we apply the flux limiting scheme to the linear convection of a square wave with the velocity component (growth rate) constant over all space. The sharp edges of the square wave test how well the scheme deals with sudden gradient changes. Figure S-4 shows the the results of the linear convection of a square wave after  $1 \times 10^5$  iterations using the different flux limiters outlined above. For reference the top left panel show the extent of convection. We see that the first-order and second-order schemes results in either a large amount of numerical (false) diffusion or the creation of unreal oscillations respectively. Such diffusivity and oscillations are typical of low order and flux unlimited schemes and highlight their inability to cope with sudden gradient changes. Fortunately, through the use of limiters this problem is quickly corrected. In all the cases where the limiters were used the results show excellent preservation of the functional form of the square wave. However, as each limiter functions slightly differently some limiters are better than others at preserving the form of the wave. Figure S-5 shows the same test simulations where the square wave is replaced by a Gaussian, which is more appropriate for the case of modelling nanocrystal growth. From the results obtained by first-order upstreaming

---

<sup>2</sup>*Round-off error* is introduced through the omission of significant figures and is associated with the computer numbering system. *Truncation error* is caused by the omission of higher order terms in the Taylor expansion of the integrals that are approximated by finite differencing.

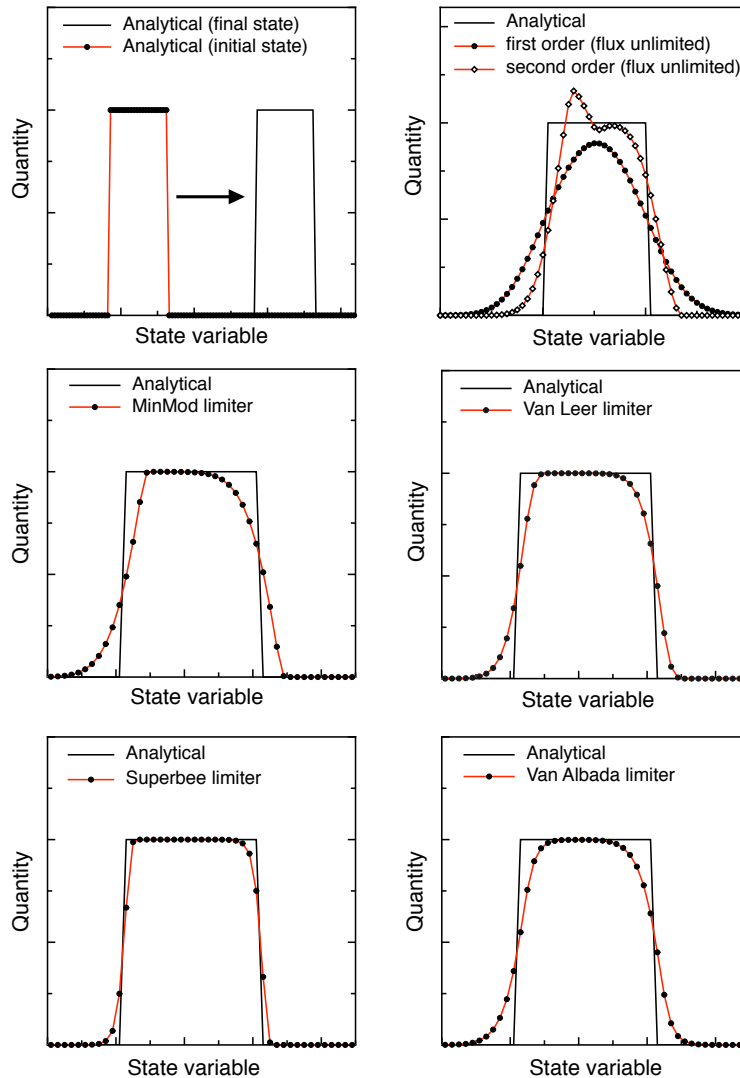


Figure S-4: Translation of a step function using various flux limiters. For reference the first-order and second-order upstream scheme with no limiter is shown (top right). 200 points 100000 time steps

(top right) we see that although the analytical and numerical positions of the maxima are almost identical the final profile has *artificially* broadened. This is important to avoid in the modelling of nanocrystals where interpretation of the results of a given simulation relies heavily on the FWHM of the distribution. The remaining four panels show the results obtained from the four limiters. Both the Van Leer and Van Albada limiters return much the same result. The MinMod limiter acts strongly on the scheme when the gradient drops below a certain value. Thus the data is seen to quickly flatten out around the peak of the Gaussian where  $2\chi < 1$ . Although the Superbee limiter copes excellently with sharp gradients, as seen in Figure S-4, it perhaps deals *too* well

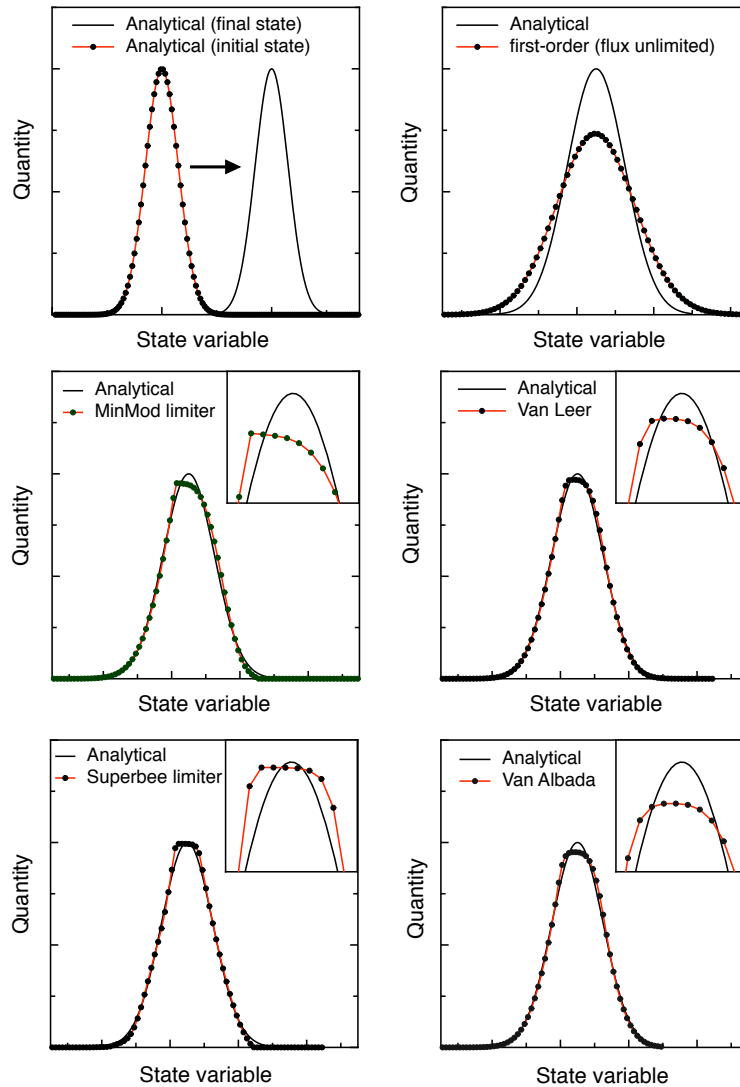


Figure S-5: Translation of a Gaussian function using various flux limiters. For reference the first-order upstream scheme with no limiter is shown (top right). 200 points 100000 time steps

when operating on smoother profiles. Through the use of all the limiters (except perhaps for the MinMod limiter), the position of the maximum value of the Gaussian is preserved as is its FWHM and amplitude. From analysis of the information presented in Figure S-4 and Figure S-5 we may now implement the scheme with confidence in the obtained values. Given its low diffusivity and ability to cope well with smooth profiles the Van Leer limiter was chosen for the simulations of NC formation and growth.

## Flow-chart of Program

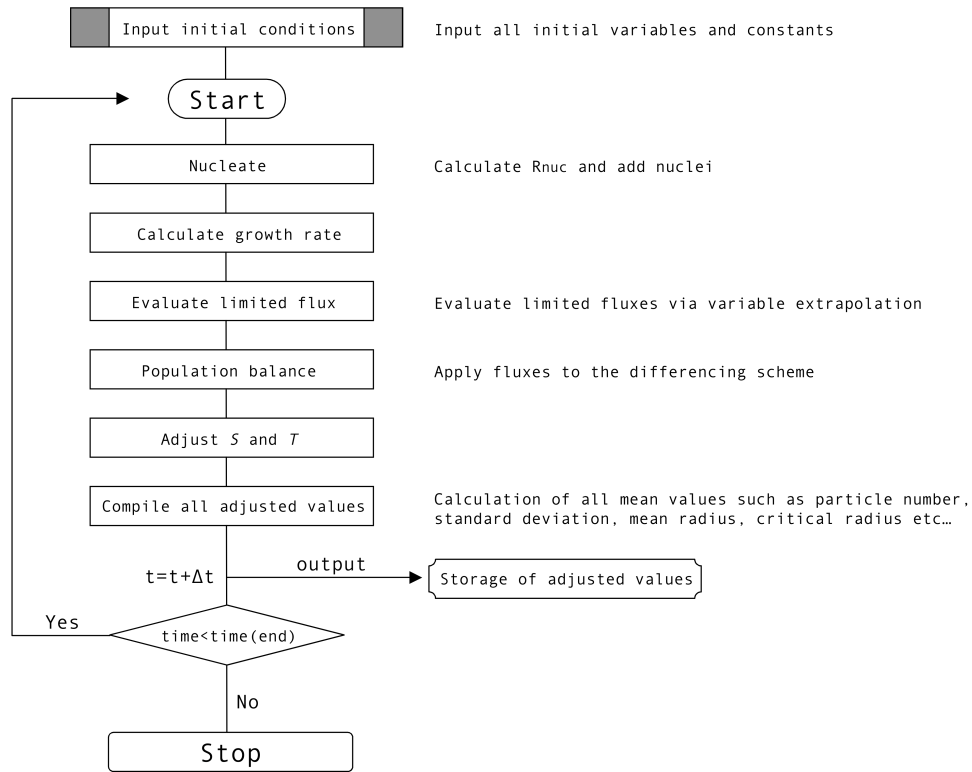


Figure S-6: Flow-chart showing the basic order of the computer program employed to solve the population balance equation.